



Tight-reservoir micropore formation and evolution in sedimentary organic-matter-bearing tuff: a case study from the Permian Tiaohu Formation in the Santanghu Basin, NW China

J. Ma & Z. Huang

To cite this article: J. Ma & Z. Huang (2016) Tight-reservoir micropore formation and evolution in sedimentary organic-matter-bearing tuff: a case study from the Permian Tiaohu Formation in the Santanghu Basin, NW China, Australian Journal of Earth Sciences, 63:4, 485-501, DOI: [10.1080/08120099.2016.1219876](https://doi.org/10.1080/08120099.2016.1219876)

To link to this article: <http://dx.doi.org/10.1080/08120099.2016.1219876>



Published online: 26 Sep 2016.



Submit your article to this journal [↗](#)



Article views: 26



View related articles [↗](#)



View Crossmark data [↗](#)

Tight-reservoir micropore formation and evolution in sedimentary organic-matter-bearing tuff: a case study from the Permian Tiaohu Formation in the Santanghu Basin, NW China

J. Ma and Z. Huang

State Key Laboratory of Petroleum Resource and Prospecting, China University of Petroleum, Beijing 102249, China

ABSTRACT

Recently, a tuffaceous tight oil reservoir with considerable reserves has been found in the Santanghu Basin, northwestern China. The physical properties of the tuff are characterised by high porosity (5–25%) and low permeability (0.01–0.50 mD). This reservoir has the peculiar property of being a sedimentary organic-matter-bearing tuff formed by air-fall volcanic ash in a lake. Its discovery offered an excellent opportunity to further our knowledge of the formation and evolution of tuffaceous tight-reservoir micropores. This study integrates analyses of organic geochemistry, thin-sections, scanning electron microscopy, CT scanning, mineral and element compositions, mercury injections and measurements of porosity and permeability to determine the characteristics of the formation and evolution of the tuff micropores. (1) The tuff reservoir comprises vitric, crystal-vitric, pelitic and silicified tuffs, which are characterised by high porosity and big throat, moderate porosity and thin throat, low porosity and thin throat, and very low porosity and moderate throat pore structures, respectively. (2) Of the four types, vitric tuff has the properties best suited to a reservoir, and devitrification of volcanic glasses is the principal mechanism of reservoir micropore formation. (3) The tuff of the Permian Tiaohu Formation contains sedimentary organic matter, and organic acids produced during kerogen maturation facilitate the process of devitrification. (4) Evolution of tuff porosity depends mainly on the original composition and burial depth. The porosity of vitric tuff is higher than crystal-vitric tuff at the same depth, but both their porosities initially decrease and then increase with depth. At depths >3000 m, vitric tuff retains the trend towards higher porosity, whereas the porosity of crystal-vitric tuff remains largely unchanged or even decreases. The results of this investigation could be considered a reference regarding the distribution and prediction of tuffaceous reservoirs in similar situations in other parts of the world.

ARTICLE HISTORY

Received 31 January 2016
Accepted 19 July 2016

KEYWORDS

Tuff; tight reservoir;
micropore; devitrification;
Tiaohu Formation;
Santanghu Basin

Introduction

As global demand for oil and gas rises and output from conventional sources decreases, the development potential of unconventional sources of hydrocarbons has become the focus of attention. Using horizontal drilling and multi-stage fracturing technology, shale reservoirs have yielded large amounts of gas and the same technology has been applied to tight reservoirs with low porosity and permeability, e.g. the Bakken Formation in Williston Basin in the United States (Fic & Pedersen, 2013). Tight oil generally refers to accumulations of petroleum in tight sandstones and carbonates (Clarkson & Pedemen, 2011; Jia, Zou, Li, Li, & Zheng, 2012b), and following the rapid expansion in shale gas extraction, it has become the most active field of hydrocarbon exploration and development in the world (Jia, Zheng, & Zhang, 2012a; Kuhn, di Primio, Hill, Lawrence, & Horsfield, 2012). However, there is considerable difference between the tight oil of the Permian Tiaohu Formation in the Santanghu Basin and the tight oil that has been discovered in other areas; the reservoir is a tight

tuff, not shale, sandstone or carbonate. Nevertheless, the tight oil of the Tiaohu Formation is within a tight reservoir that requires fracturing for commercial productivity. Tuffs are formed by volcanic ash during volcanic eruptions (Gong, Ni, & Lu, 2010). Explosive volcanic eruptions can produce large amounts of fine-grained pyroclastic material, which may be spread laterally over large areas by wind drift (Huff, 2008; Kolata, Frost, & Huff, 1987; Königer, Lorenz, Stollhofen, & Armstrong, 2002; Qiu et al., 2014). Sedimentation occurs either when the tuffaceous material falls directly into a lake ('primary airfall type'), or when it is transported into a lake by water ('water carrying resedimented type') (d'Atri, Dela Pierre, Lanza, & Ruffini, 1999; Haaland, Furnes, & Martinsen, 2000; Qiu, Liu, Mao, & Wu, 2011). The tuff of the Tiaohu Formation formed mainly from volcanic ash that was deposited directly into the lake without weathering and extensive transportation. Rapid accumulation of the volcanic ash, accompanied by buildup of polluting gases, led to the death of aquatic organisms, which contributed to the sedimentary organic matter to the tuff. However, periods of volcanic dormancy allowed aquatic

organisms to become re-established, leading to renewed enrichment of the organic matter (Li, Li, Huang, Wang, & Wang, 2014; Wang, Pan, & Wei, 2011). As a special type of tight oil reservoir, research on sedimentary organic-matter-bearing tuff has been limited, but it is of great scientific significance. The formation and evolution of tuffaceous tight-reservoir micropores are related directly to the prediction of effective tuff reservoirs. Therefore, it is of considerable importance to investigate their characteristics, to provide an in-depth analysis of formation mechanisms and for guiding their exploration.

Geological setting

Located in the northeastern part of the Xinjiang Uygur Autonomous Region of China, the Santanghu Basin is bordered by the Republic of Mongolia to the north, Turpan-Hami Basin to the south, and Junggar Basin to the west. Sandwiched between the Altai and Tianshan mountains, the Santanghu Basin is a superimposed basin developed on an early Paleozoic basement (Liu, Li, & Zhu, 2010). Aligned NW–SE, it is about 500 km long and 40–70 km wide, covering an area of $\sim 2.3 \times 10^4$ km². The basin can be divided into three tectonic units: the NE thrust-fold belt, central depression and SW thrust-fold belt (Xu, Tang, & Zhang, 2013). The central depression comprises four uplifts and five sags of which the Malang Sag, covering an area of ~ 1800 km², is the most important secondary structural unit. This unit has received considerable attention, which is why it was selected as the focus of this study (Figure 1a). The Santanghu Basin was an intraplate rift basin during the Permian (Xiao et al., 2004a; Xiao, Zhang, Qin, Sun, & Li, 2004b). The Lucaogou and Tiaohu formations developed during a period of volcanism. The volcanism was weak during the deposition of the Lucaogou Formation, during which mudstones, lime mudstones, dolomitic mudstones and other fine-grained lacustrine sediments developed, forming excellent source rocks (Gao, Li, & Liang, 2010; Ma, Huang, Li, & Wu, 2012). However, the volcanism was more intense when the first member of the Tiaohu Formation was deposited (Zhu, Zhang, Gu, & Guo, 2005). This led to the formation of a several hundred metre-thick basalt layer over most parts of the basin with local diabase invasions. Subsequently, as the volcanism weakened, a 30 m-thick tuff was deposited at the bottom of the second member of the Tiaohu Formation, which is the main tight reservoir in the Malang Sag. The tuff reservoir contains abundant oil, and many wells have achieved high-yield oil flows after fracturing. Normal lacustrine sediments, consisting mainly of 400 m-thick (or more) tuffaceous mudstones and mudstones, were deposited onto the tuff. The tight reservoirs, which are not controlled by structures, are distributed mainly within the current lower location of the structure (depression) and slope of the Malang Sag (Figure 1b).

The intermediate–acidic tuff of the Tiaohu Formation, formed at the end of a cycle of volcanic eruptions, is distributed on a set of stable mafic–intermediate volcanic rocks (mainly basalt). They are the product of the evolution from

basic magma to acid magma and from strong volcanic activity to weak volcanic activity. The first and second members of the Tiaohu Formation were formed during a complete cycle of volcanic eruptions, which developed thick sedimentary rocks at the end of the second member. The third member of the Tiaohu Formation was formed during another cycle of volcanic eruptions. Mafic minerals crystallise and separate during the process of magma ascent along volcanic conduits. Thus, the content of SiO₂ in acidic magma becomes higher, which means the magma becomes more viscous and its flow capacity decreases. Energy accumulates following the blockage of the crater, giving rise to powerful eruptions and to the formation and distribution of volcanic ash that forms tuffs through the processes of consolidation and compaction.

The volcanic ashes were derived from the volcanic activity belt (crater) and tuff distribution was controlled by both the volcanic activity belt and the sedimentary paleotopography. Crystal-vitric tuff is usually distributed near the volcanic activity belt, vitric tuff is usually further away, in depositional depressions on either side, and tuffaceous mudstones and pelitic tuffs are found in the deep lake (Figure 2). In the northwest and southwest of the Malang Sag, tuffaceous siltstone and tuffaceous glutenite developed, respectively, because of the influence of terrigenous clastics. The tuffaceous tight oil reservoirs discovered are distributed mainly in the vitric tuff lithofacies on both sides of the volcanic activity zone.

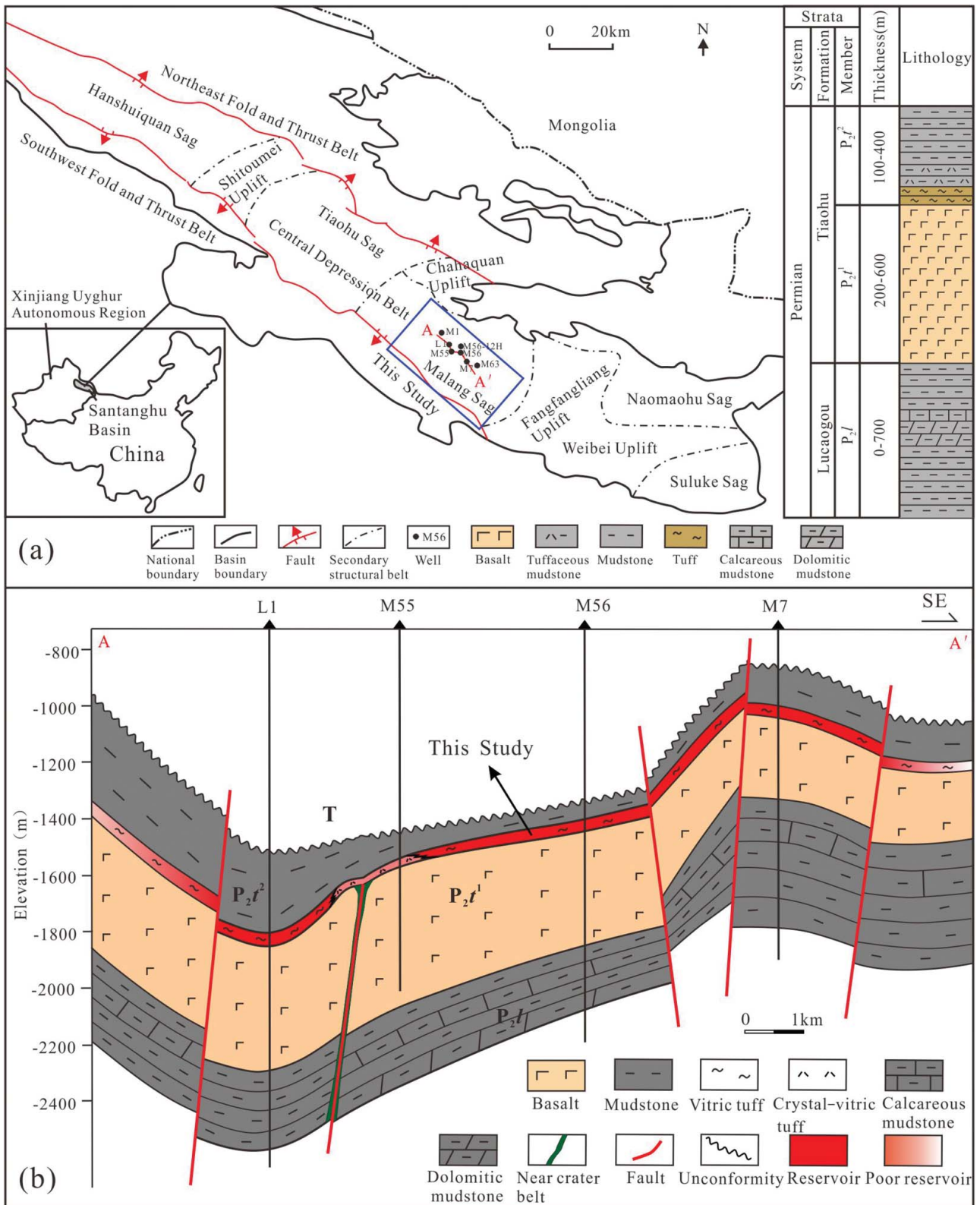
Samples and methods

Sample selection

Cores were obtained from nine existing drilling wells in the Malang Sag. Samples for tests of porosity, permeability and pore throat structures were obtained from horizontal core plugs (2.5 × 5 cm) drilled parallel to the bedding plane; because they are oil-bearing, the tuff samples were subjected to an oil-wash treatment prior to testing. Analyses of the organic geochemistry, thin-sections, scanning electron microscopy (SEM), CT scanning, pore throat structures, and petrophysical properties (porosity and permeability) of the tuffs were undertaken at the State Key Laboratory of Petroleum Resource and Prospecting, China University of Petroleum, Beijing. X-ray diffraction (XRD) analysis of the whole-rock minerals and elemental analysis were performed at the Micro Structure Analytical Lab of Peking University.

Analysis of organic geochemistry

Pyrolysis analysis of 34 core samples was performed with Rock-Eval. Measured parameters included S₁ (free hydrocarbons), S₂ (hydrocarbons cracked from kerogen), S₃ (carbon dioxide released from organic matter), and T_{max} (temperature of maximum yield of pyrolysate). The total organic carbon (TOC) was determined using a CS230HC organic carbon analyser. The measurement technique was based on the combustion of the sample in an oxygen atmosphere to convert the



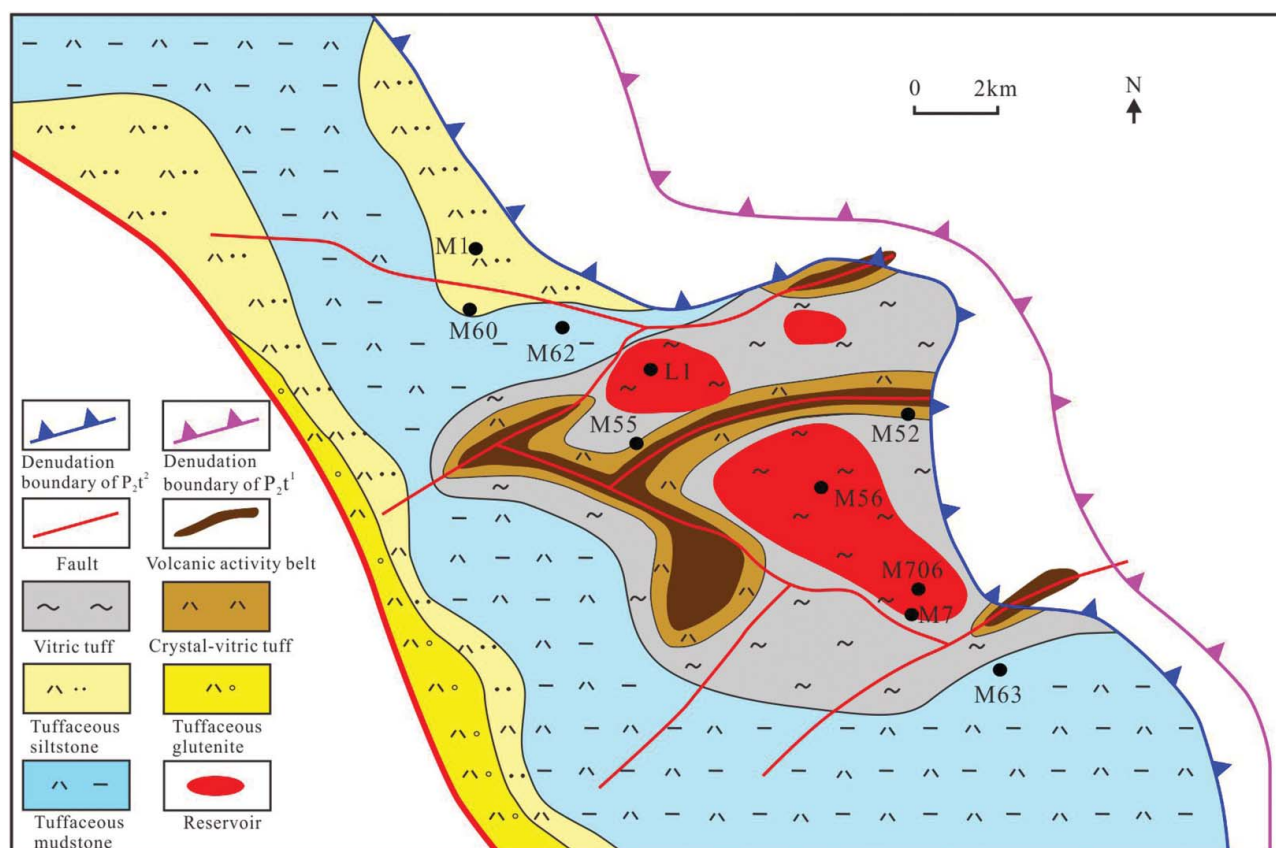


Figure 2. Lithofacies and reservoir distribution of the Tiaohu Formation tuffs in the Malang Sag, NW China, showing reservoirs distributed mainly in the lithofacies zone of the vitric tuff on both sides of the volcanic activity zone.

TOC to CO_2 , following which the hydrogen index (HI) was calculated with S_2 and TOC.

Analysis of reservoir characteristics

Small samples of massive tuff were selected for thin-section analysis, and their fresh surfaces coated with gold. The morphologies and pore types of the tuff samples were observed using a high-resolution field emission scanning electron microscope (FEI Quanta200) combined with secondary electron, Ar-ion-beam milling and backscattered electron imaging. For CT scanning, tuff samples were cut into small plugs (1×10 mm), and micropores were observed using Xradia Micro CT-400 with 60–140 keV X-ray source and 0.8–1 μm resolution. Three-dimensional reconstruction of the image was completed in reconstructor software, and identification and calculation of the porosity was conducted using threshold technology. The tuff core samples were crushed to sizes of <40 μm using a mortar and their mineral composition determined by XRD analysis with the following parameters: Cu-K α radiation, 40 kV voltage, 100 mA current, 3–70° scanning range, 0.01° sampling step width, and 4°/min scanning speed. Minerals were recognised according to the diffractogram and their relative abundances (wt%) were analysed semi-quantitatively. Analyses of the major elements of the tuffs were conducted using X-ray fluorescence. Porosity and permeability were tested using helium and nitrogen, respectively, with the

gas-testing method (PDP-200). The parameters of pore throat structures of the tuffs were tested using a high-pressure mercury injection meter (PoreMaster GT60).

Results

Geochemical characteristics of sedimentary organic matter in tuffs

Direct measurements of the TOC of the tuff samples cannot indicate the abundance of sedimentary organic matter because the Tiaohu Formation tuff is an oil-filled reservoir. Thus, the crude oil or bitumen within the rocks has to be extracted completely, prior to evaluating the hydrocarbon potential of the tuff. The TOC of the tuffs in the second member of the Tiaohu Formation reflects the low abundance (0.5–1.0 wt%) of sedimentary organic matter (Figure 3a). The total hydrocarbon yield ($S_1 + S_2$) is mainly 2–6 mg/g (Figure 3b) and HI values are 20–336 mg HC/g TOC (average: 154 mg HC/g TOC) (Ma, Huang, Gao, & Chen, 2015). A plot of HI vs pyrolysis T_{max} , which is usually used to classify the maturity and type of organic matter (Tissot & Welte, 1984), shows that the organic matter in the samples is predominantly Type III and II₂ kerogen, although a few samples are Type II₁ kerogen (Figure 3c). The T_{max} values vary primarily from 420 to 450°C, indicating that the organic matter is in the window of the mature oil stage.

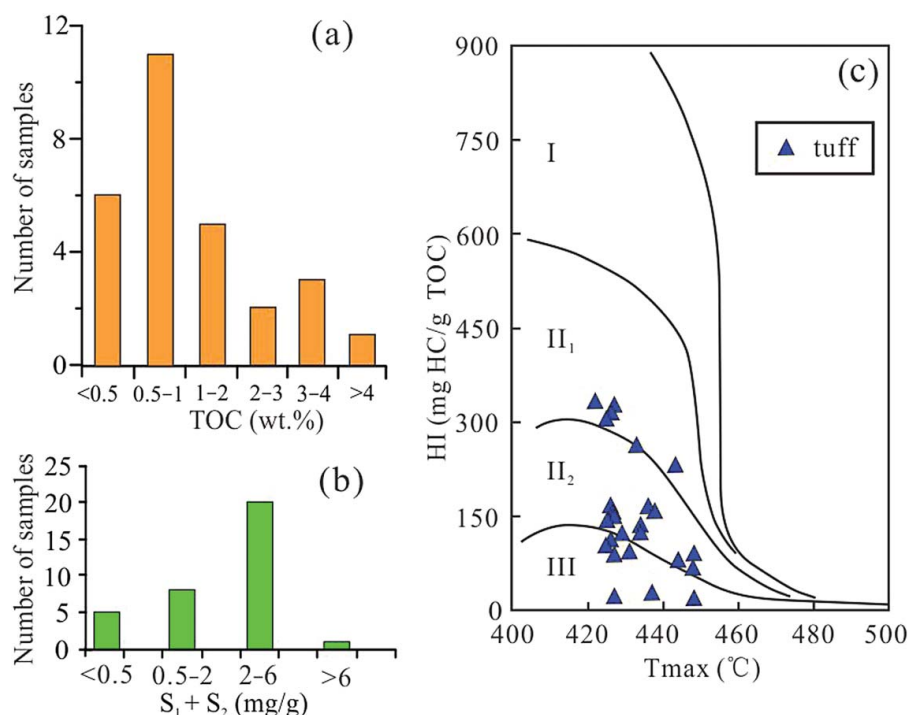


Figure 3. Geochemical characteristics of tuff samples from the Tiaohu Formation after extraction. (a) Total organic carbon (TOC) distribution, showing the organic matter abundance of the tuffs. (b) Hydrocarbon yield ($S_1 + S_2$) distribution, showing the hydrocarbon-generating potential of organic matter in the tuff. (c) Plot of the hydrogen index (HI) vs the temperature of maximum yield of pyrolysate (T_{max}) showing the kerogen types.

Tuff types and mineral composition

Generally, the crystal pyroclast content within the tuff increases with proximity to the crater. Further from the crater, the vitric composition of the tuff increases (Thompson & Hermes, 1990). However, at even greater distances from the crater, pelitic tuff or tuffaceous mudstone are found because of the insufficient supply of volcanic ash and increasing content of shale (Jiao, Liu, Zhang, Feng, & Wu, 2014; Liang et al., 2014). Based on distance from the volcanic activity belt, compositional differences and microscopic characteristics, the tuff can be divided into vitric, crystal-vitric, pelitic and silicified in this area. These four types of tuff constitute the tuff reservoir section, which has certain regularity in its longitudinal distribution (Figure 4).

Vitric tuff. Vitric tuff, formed at the early stage of the end of a volcanic eruption cycle, is generally distributed further from the volcanic activity belt and vertically within the central-lower part of the tuff. It consists mainly of mixed deposits of vitroclasts with small amounts of fine crystal pyroclasts, and a high degree of devitrification (Figure 5a, b). Very small quartz and feldspar particles (mostly $<3 \mu\text{m}$) comprise the main mineral composition, and clay mineral content is low, generally $<10 \text{ vol\%}$ (Table 1). The clay minerals are formed by devitrification, rather than being terrigenous matter, and they are mainly cleavage-sheet chlorite dispersed between the quartz and feldspar particles.

Crystal-vitric tuff. Crystal-vitric tuff, interbedded with vitric tuff, is generally distributed near the volcanic activity belt and

vertically within the central-lower part of the tuff. Although it consists mainly of vitroclasts, particles of crystal pyroclasts, characterised by stripes of marginal directional arrangement, are large, and their content is higher than in vitric tuff (Figure 5c). Large crystal pyroclasts cannot move far and thus, they are deposited near the volcanic activity belt. The distribution of crystal pyroclasts is also controlled by volcanic eruption intensity. Crystal pyroclasts form a ring-shaped belt or fan-shaped distribution around the crater, and their subsequent distributions will be more or less than the original range, depending on the strength of the following volcanic eruptions. Volcanic eruptions of different strength thus form vertically interbedded layers of vitric and crystal-vitric tuff with different thicknesses. Crystal-vitric tuff is characterised by higher content of quartz and feldspar, and lower of clay minerals (generally $10\text{--}30 \text{ vol\%}$). The source of clay minerals is the same as in vitric tuff, but the content of mixed-layer illite/smectite is clearly increased (Figure 5d).

Pelitic tuff. Pelitic tuff is generally distributed far from the volcanic activity belt and vertically within the upper part of the tuff. Terrigenous shale content is relatively high, and the tuff is very tight (Figure 5e, f). Pelitic tuffs are deposited far from the crater, associated with weak volcanic activity, and the presence of terrigenous argillaceous clastics. The content of clay minerals is high, generally $>15 \text{ vol\%}$.

Silicified tuff. Thin silicified tuff is generally distributed far from the volcanic activity belt and vertically within the bottom of the tuff, where it has direct contact with the lower

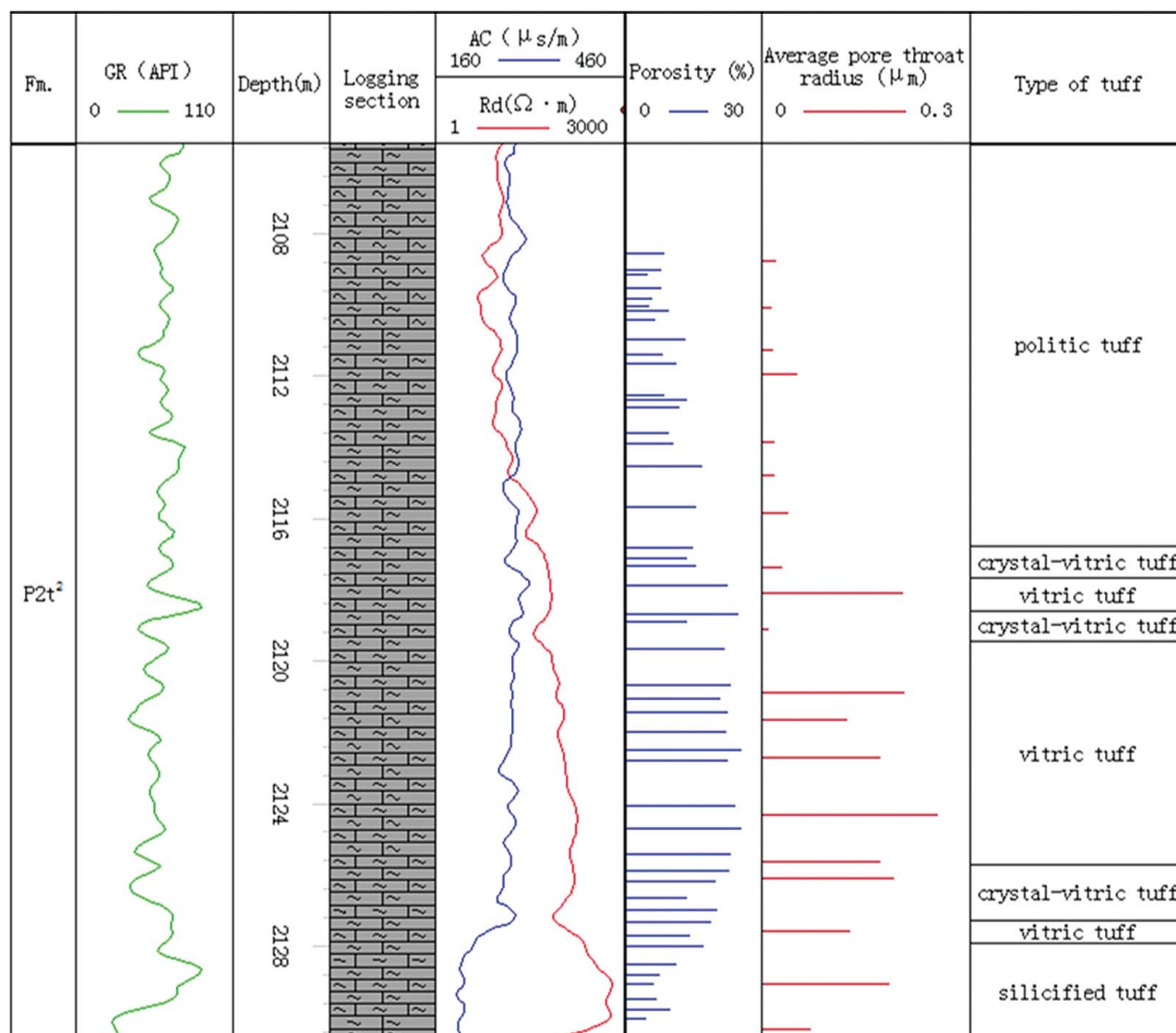


Figure 4. Vertical distribution characteristics of different types of tuffs (an example from Well M56-12H).

basalt. Predominantly, it consists of vitroclasts and small amounts of crystal pyroclasts, but it is characterised by silicification with continuous amorphous SiO_2 (Figure 5g, h). This type of tuff is very tight, and thus its resistivity on the well-logging curve is extremely high, usually $>300 \Omega \cdot \text{m}$. Located at the transition zone between the tuff and lower tight basalt, downward fluid exchange is blocked during the process of devitrification, and SiO_2 is precipitated because of the very high concentration. Therefore, silicified tuff is formed because the devitrification pores are cemented by the amorphous SiO_2 .

Physical properties and pore types of the reservoir

Reservoir physical properties. Physical properties of the tuff directly determine reservoir quality. Statistical results of 86 porosity and permeability data from the sedimentary organic-matter-bearing tuff of the Tiaohu Formation, show the tuff

reservoir is characterised by moderate–high porosity (10–25%; Figure 6a) and low permeability (air permeability <1.0 mD, mainly 0.01–0.50 mD; Figure 6b). A positive relationship exists between porosity and permeability, but it is not a linear. Although the greater the porosity, the higher the permeability is; the relationship is complex.

The physical properties of different types of tuff vary. The porosity and permeability of vitric, crystal-vitric, and both pelitic and silicified tuffs are usually $>18\%$ and >0.1 mD, 10–18% and <0.1 mD, and $<10\%$ and <0.01 mD, respectively. Vitric tuff has the properties best suited to a reservoir.

Pore types. Pores are difficult to observe in the thin-sections of tight sedimentary organic-matter-bearing tuff. However, well-developed micropores can be found under SEM and CT scanning. The sizes of the individual pores are small but they are present in large numbers. Pore size is mainly on the micron–nanometer scale (Figure 7), and for the sake of

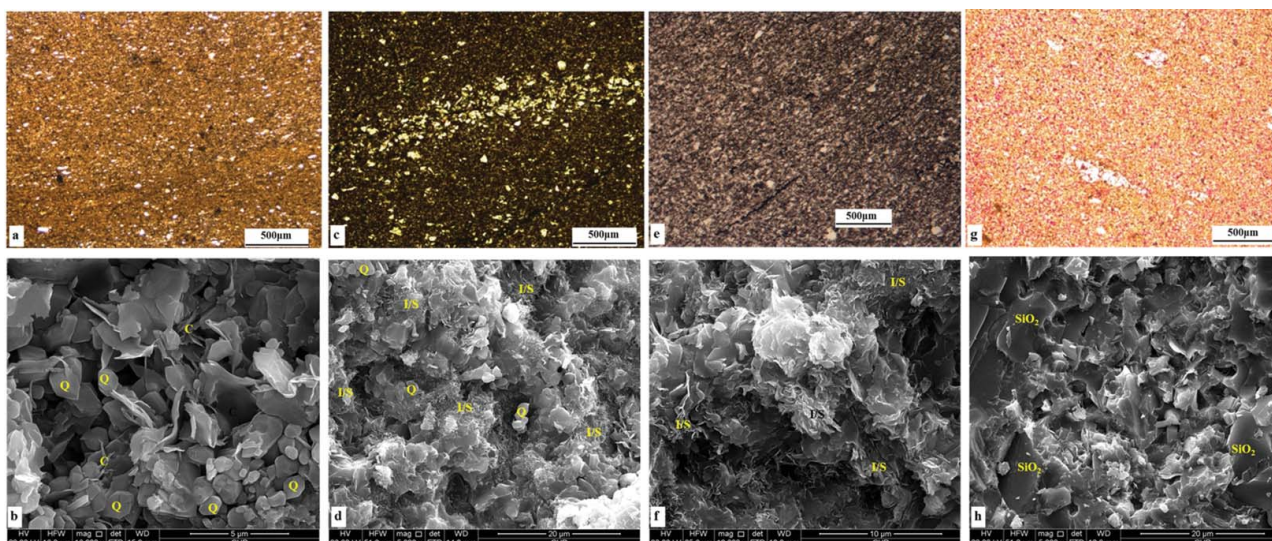


Figure 5. Petrographic characteristics of different types of the Tiaohu Formation tuffs in the Santanghu Basin. (a) Vitric tuff. Core of Well M7, 1970.87 m. Thin-section. (b) Vitric tuff. Core of Well M56, 2143.3 m. Observed by FEI-SEM. (c) Crystal-vitric tuff. Core of Well M56-15H, 2252.34 m. Thin-section. (d) Crystal-vitric tuff. Core of Well M55, 2268.25 m. Observed by FEI-SEM. (e) Pelitic tuff. Core of Well M56-12H, 2110.2 m. Thin-section. (f) Pelitic tuff. Core of Well M56-15H, 2248 m. Observed by FEI-SEM. (g) Silicified tuff. Core of Well M56-12H, 2131.12 m. Thin-section. (h) Silicified tuff. Core of Well M56-12H, 2131.12 m. Observed by FEI-SEM.

uniformity, the pore size classification of Loucks, Reed, Ruppel, and Hammes (2012) for unconventional shale is used here. Zhao, Li, Jiang, Zhang, and Li (2013) also adopted this standard in their study of the pore types of organic-matter-rich calcilutite. Matrix-related pores in tuffs can be divided into

two types: (1) interparticle pores between minerals (mainly quartz and feldspar); and (2) intraparticle pores within minerals (mainly feldspar, inorganic minerals and clay). In this study, most of the interparticle and intraparticle pores were formed by devitrification, and thus these types of pores are referred

Table 1. Relative contents of different minerals in the Tiaohu Formation tuffs from X-ray diffraction analysis.

Well	Depth (m)	Lithology	Relative content of minerals (%)				
			Quartz	Potassium feldspar	Albite	Clay minerals	Calcite
L1	2547.86	Vitric tuff	75	—	16	7	2
L1	2548.78	Vitric tuff	76	6	8	4	6
L1	2548.70–2548.80	Vitric tuff	56	—	20	9	15
L1	2548.90	Vitric tuff	47	—	15	11	27
M56	2141.60–2141.80	Vitric tuff	63	—	33	—	4
M56	2142.20–2142.30	Vitric tuff	57	—	36	—	7
M56	2142.50–2142.60	Vitric tuff	51	—	35	4	10
M56	2142.80–2142.96	Vitric tuff	67	—	29	4	—
M56	2143.60–2143.70	Vitric tuff	43	—	42	9	6
M56	2144.10–2144.40	Vitric tuff	49	—	46	5	—
M56	2144.90–2144.60	Vitric tuff	32	—	58	—	10
M56	2144.73	Vitric tuff	69	—	19	4	8
M56	2145.30–2145.40	Vitric tuff	36	—	57	4	3
M7	1790.80–1790.90	Vitric tuff	66	—	9	14	11
M7	1885.06	Vitric tuff	57	—	37	6	—
M56-12H	2118.20–2118.30	Vitric tuff	52	—	36	12	—
M56-12H	2118.90–2119.10	Vitric tuff	68	—	28	4	—
M56-12H	2122.40–2122.60	Vitric tuff	45	—	38	17	—
M55	2269.15–2269.25	Crystal-vitric tuff	40	—	24	13	23
M55	2270.33–2270.48	Crystal-vitric tuff	45	—	21	28	6
M55	2281.00	Crystal-vitric tuff	41	11	17	31	—
M56-15	2252.40	Crystal-vitric tuff	43	10	34	10	3
M56-12H	2110.86–2111.07	Pelitic tuff	56	—	28	16	—
M56-12H	2116.66–2116.76	Pelitic tuff	38	—	19	43	—
M62	2379.00–2379.16	Pelitic tuff	9	—	55	21	15
M62	2381.29–2381.42	Pelitic tuff	45	5	18	26	6
M56-12H	2131.10	Silicified tuff	53	13	30	2	2
M56-12H	2131.12	Silicified tuff	72	—	21	3	4
M56-15H	2268.80	Silicified tuff	58	13	22	7	—
M56-15H	2268.81	Silicified tuff	50	7	30	13	—

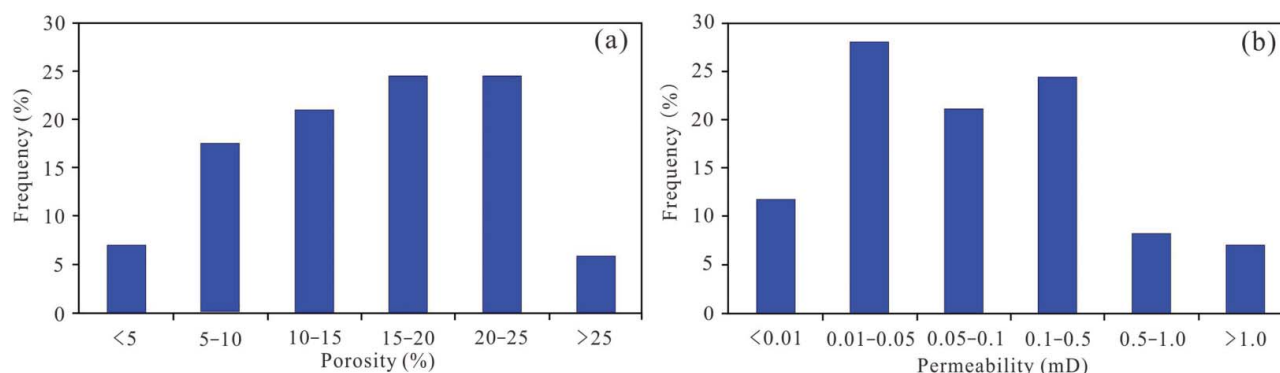


Figure 6. Distributions of (a) porosity and (b) permeability of the tuffs of the Tiaohu Formation showing the tuffs are characterised by moderate–high porosity and low permeability.

to collectively as devitrification pores (Zhao, Huang, Wang, & Di, 2009).

(1) Interparticle pores

Analysis of the petrographic characteristics of the Tiaohu Formation tuffs reveals a relatively simple mineral composition that comprises mainly quartz and feldspar. The interparticle pores formed by devitrification are found mainly between the quartz and feldspar and they can be observed clearly using SEM (Figure 7c). Interparticle pores are most common in vitric tuff, followed in descending order by crystal-vitric, pelitic and silicified tuffs.

(2) Intraparticle pores

Intraparticle pores in the Tiaohu Formation tuffs comprise dissolution pores within feldspar grains, intercrystalline pores within a pyrite framboid, and pores within the clay minerals. It is common for dissolution intraparticle pores to form within feldspar grains produced by devitrification and crystal fragments of feldspar in tuffs (Figure 7d). Energy dispersive spectrometer analysis shows that the major mineral composition, within which such dissolution intraparticle pores developed, is mainly O, Si, Al and Na. Pyrite also developed in the tuff, demonstrating that it formed in a reducing environment. The pyrite framboids include many pyrite crystals, among which many micropores act as storage space (Figure 7e). Although the content of clay minerals in the tuff is very low, the main clay mineral is chlorite, which is in the form of cleavage-sheet shapes with micropores developed between them (Figure 7f).

Characteristics and types of tuff micropore structures

Pore-structure characteristics. Pore structures measured by the mercury injection method reflect the number, size, form, distribution and connectivity of reservoirs (Ma, Li, & Liu, 2005). Pore-structure parameters can be divided roughly into three categories: maximum radius, average radius and radius of median saturation, which indicate the size of the pore throat. Displacement pressure, pressure of median saturation,

maximum mercury injection saturation and mercury withdrawal efficiency can be used to determine the connectivity of pore throats. Pore structure parameters of 58 tuff samples are shown in Table 2, and summarised below.

Maximum pore throat radius ranges from 0.013 to 0.835 μm (average: 0.205 μm), average radius from 0.003 to 0.286 μm (average: 0.085 μm), and the radius of median saturation from 0.004 to 0.368 μm (average 0.090 μm). From these data, pore throat radius is shown to be <1.0 μm (generally <0.5 μm), indicating micropores.

Pore throat skewness ranges mainly from 0.07 to 12.8 (average: 1.9) and the sorting coefficient ranges mainly from 0.004 to 0.325 (average: 0.074), indicating that the pore throats are well sorted.

The displacement pressure of the tuffs ranges mainly from 0.88 to 58.20 MPa (average: 11.35 MPa), the pressure of median saturation from 2.0 to 188.6 MPa (average: 36.9 MPa), the maximum mercury injection saturation from 54.1 to 99.1% (average: 87.9%), and the mercury withdrawal efficiency from 0.00 to 51.04% (average: 25.10%). The high displacement pressure indicates that the tuff has small pore throats, however, the pore throats are connected because both the maximum mercury injection saturation and the mercury withdrawal efficiency are high.

Pore-structure types. Pore structures of the Tiaohu Formation tuffs can be divided into four types (below), which correspond to the four types of tuff, and there is a good correlation between the average pore throat radius and porosity (Figure 8).

(1) High porosity and big throat type

The line segment of the mercury injection curve (Figure 9a) is long, and the slope is small, showing that the throats have a centralised distribution. Combined with low displacement pressure and high mercury withdrawal efficiency (mainly 40–51%), this indicates the good pore structure of the tuff. Porosity is high, mostly >18%. This type of pore structure usually appears in vitric tuffs. High vitroclast content leads to a large number of devitrification pores. Good connectivity of

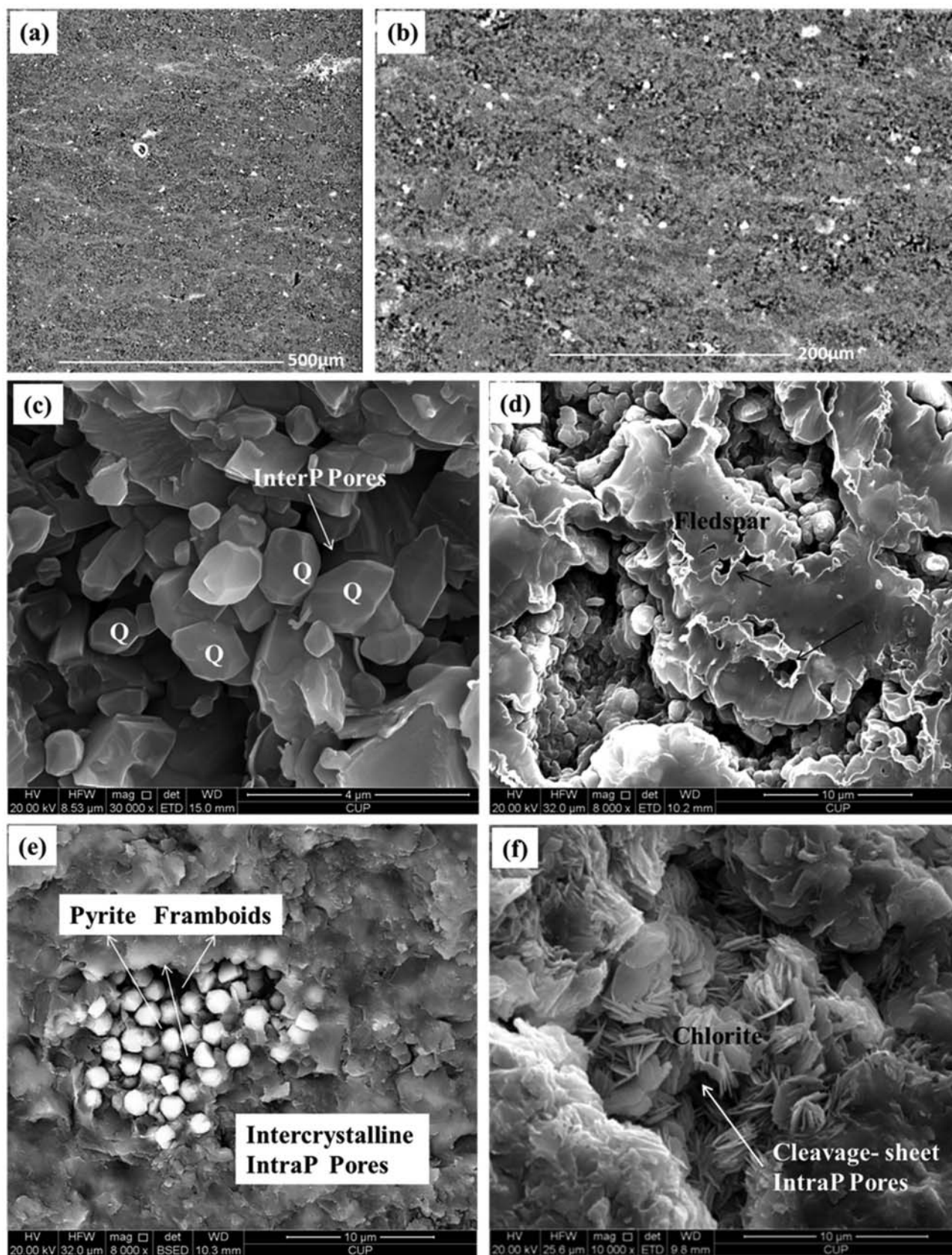


Figure 7. Example of different micropores in the tuffs of the Tiaohu Formation. (a, b) Micropores observed by CT scanning, Well M56-12H, 2118.4 m. (c) Interparticle (InterP) pores between quartz grains caused by devitrification. Well M56, 2143.3 m. Observed by FEI-SEM. (d) Dissolution intraparticle (IntraP) pores within a large feldspar grain. Well M56, 2143.3 m. Observed by FEI-SEM. (e) Intercrystalline IntraP pores within a pyrite framboid. Well L1, 2548.7 m. BSED image. (f) Cleavage-sheet IntraP pores within chlorite. Well M56, 2142.5 m. Observed by FEI-SEM. Abbreviations: det = detector; WD = working distance; mag = magnification; HV = high voltage; HFW = horizontal frame width; spot = spot size; BSED = backscattered electron detector.

Table 2. Pore structure parameters of typical tuff samples.

Well	Depth (m)	Type	Porosity (%)	Size of pore throat			Sorted behaviour of pore throat			Connectivity of pore throat		
				Average pore throat radius (μm)	Maximum pore throat radius (μm)	Pore throat radius of median saturation (μm)	Sorting coefficient	Skewness	Mercury withdrawal efficiency (%)	Maximum mercury injection saturation (%)	Displacement pressure (MPa)	Pressure of median saturation (MPa)
M56	2141.97–2142.18	A	24.4	0.101	0.161	0.100	0.05	0.79	16.71	95.14	4.56	7.32
M56-15H	2248.27–2248.39	A	23.1	0.104	0.322	0.041	0.08	0.69	36.73	90.57	2.28	17.80
M56-12H	2121.69–2121.86	A	22.9	0.205	0.311	0.224	0.08	0.26	51.04	93.70	2.36	3.28
M56	2143.53–2143.61	A	22.9	0.111	0.237	0.109	0.07	0.58	29.93	96.17	3.10	6.72
M56-12H	2122.44–2122.65	A	22.3	0.123	0.221	0.122	0.06	1.01	47.11	95.68	3.32	6.01
M56	2142.96–2143.08	A	21.6	0.122	0.225	0.123	0.07	0.15	32.10	97.52	3.26	5.98
M56-15	2264.62–2264.83	A	20.4	0.154	0.334	0.074	0.12	0.37	40.56	94.44	2.20	10.00
M56-15H	2259.05–2259.33	A	20.0	0.214	0.448	0.203	0.14	0.07	46.16	97.30	1.64	3.62
M56-15H	2255.28–2255.46	A	19.4	0.084	0.216	0.006	0.05	0.45	20.74	93.39	3.41	118.60
M56-15H	2260.57–2260.73	A	18.5	0.044	0.105	0.007	0.02	0.61	33.76	89.10	7.00	111.60
M56-15H	2255.55–2255.78	B	17.0	0.047	0.129	0.064	0.03	1.17	32.55	95.86	5.68	11.40
M56	2144.86–2144.99	B	16.0	0.048	0.112	0.041	0.03	1.23	19.91	95.98	6.56	17.80
M56	2144.39–2144.59	B	14.3	0.012	0.048	0.008	0.01	2.20	1.95	88.76	15.40	92.40
M56-12H	2118.16–2118.29	B	13.3	0.028	0.053	0.025	0.02	1.85	19.89	95.66	13.80	28.90
M56-15H	2247.48–2247.65	B	13.1	0.003	0.013	0.114	0.01	0.68	8.12	54.06	58.20	6.44
M56-15H	2259.77–2260.05	B	12.2	0.029	0.115	0.008	0.05	0.67	6.65	84.92	6.40	90.40
M56-12H	2114.63–2114.77	C	9.4	0.018	0.036	0.015	0.02	7.16	18.04	94.67	20.60	49.20
M56-12H	2110.86–2111.07	C	5.7	0.013	0.018	0.006	0.03	7.86	12.31	82.85	41.20	128.40
M56-12H	2109.56–2109.79	C	8.5	0.019	0.037	0.013	0.03	8.50	0.00	85.45	19.90	56.30
M56-15H	2267.35–2267.53	D	8.4	0.085	0.574	0.029	0.16	2.23	19.25	68.28	1.28	25.20
M56-12H	2129.85–2129.98	D	7.2	0.182	0.557	0.101	0.22	2.99	16.88	85.90	1.32	7.28

A, vitric tuff; B, crystal-vitric tuff; C, pelitic tuff; D, silicified tuff.

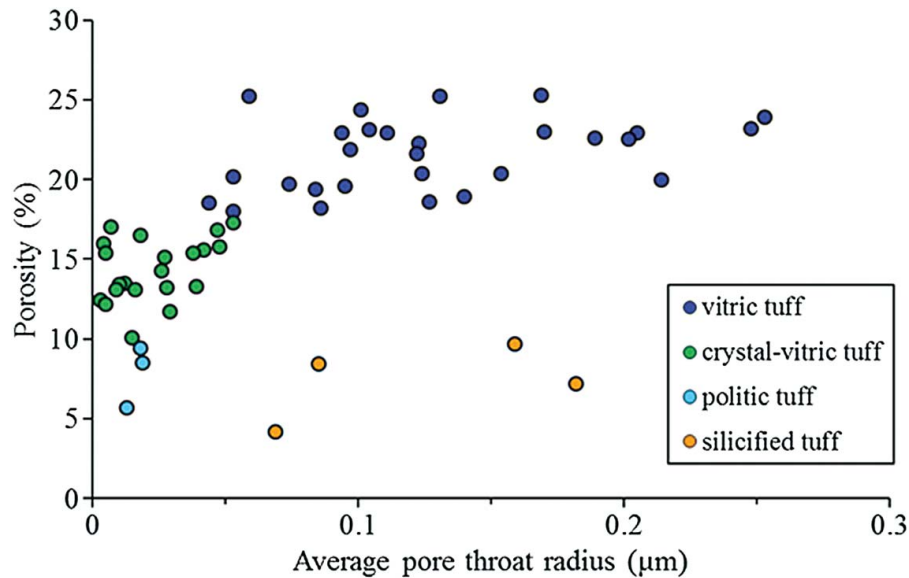


Figure 8. Plot of average pore throat radius vs porosity of the Tiaohu Formation tuffs, showing that the pore throat radius and porosity of the four types of tuff differ. Porosity is higher in tuffs with a larger pore throat radius.

adjacent devitrification pores promotes the formation of the high porosity.

(2) Moderate porosity and thin throat type

The line segment of the mercury injection curve is also long, and the slope is small (Figure 9b), showing that the throats have a relatively centralised distribution. Combined with the high displacement pressure and moderate mercury withdrawal efficiency (mainly 10–40%), indicating relatively good tuff pore structure. Porosity is moderate, ranging from 10 to 18%. This type of pore structure usually appears in crystal-vitric tuffs. Higher content of crystal pyroclasts and lower of the original matter for devitrification results in the lower porosity. High content of mixed-layer illite/smectite filling and

dividing the pores also contributes to the thin throats and moderate porosity.

(3) Low porosity and thin throat type

The line segment of the mercury injection curve is short, and the slope is large (Figure 9c). Combined with the high displacement pressure and low mercury withdrawal efficiency (mainly <20%), this reflects the poor pore structure. Porosity is mostly <10%, and it generally appears in pelitic tuffs. Devitrification is severely hindered because the high contents of terrigenous argillaceous sediments that block the pores and, therefore, the reservoir's physical properties are poor.

(4) Low porosity and moderate throat type

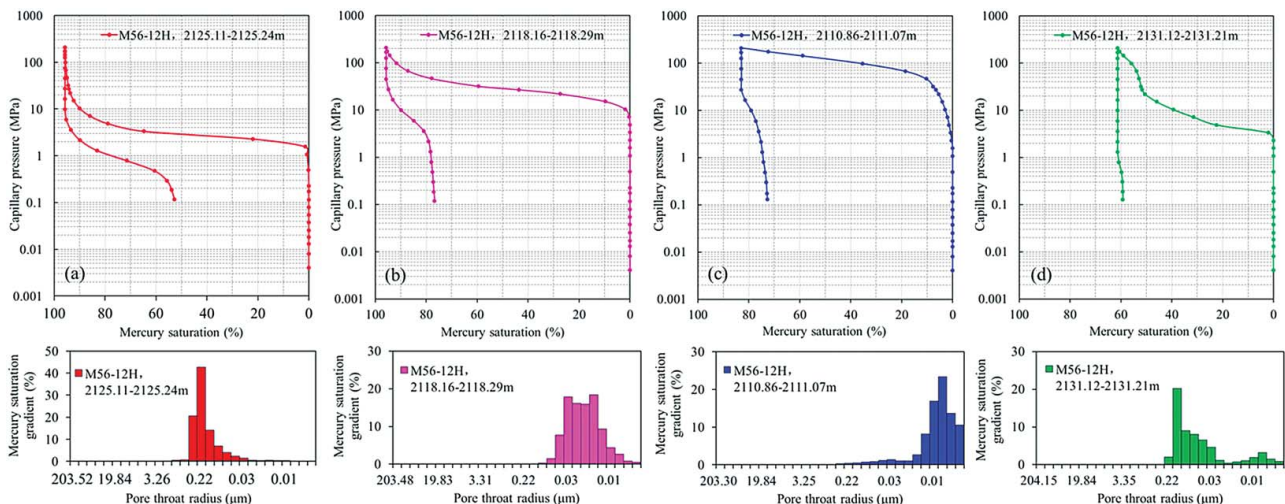


Figure 9. Characteristics of the mercury injection curves and pore throat radii distributions of different types of tuff reservoir. (a) High porosity and big throat type, (b) moderate porosity and thin throat type, (c) low porosity and thin throat type, and (d) low porosity and moderate throat type.

The line segment of the mercury injection curve of this type is short, and the slope is large (Figure 9d). Combined with the moderate displacement pressure and low mercury withdrawal efficiency (mainly <20%), this reflects the poor pore structure of the tuff. The reservoir is very tight and porosity is mostly <10%. This type of pore structure commonly appears in silicified tuffs. Because of the retention of the vitric tuff characteristics, pore throat radii are characterised by 'twin peaks' of large and small sizes and the average pore throat radius is generally >0.05 μm (Figure 9d).

Discussion

Micropore formation in the tuffs

Tuffs are formed from volcanic ash through the processes of consolidation and compaction. Volcanic glass is an integral but extremely unstable component, formed under conditions of rapid cooling of the magma, with mainly silicate composition. The strength of devitrification depends on duration, temperature and pressure during the burial process. Some components might be lost with pore water through hydrolysed devitrification, but the remaining components can be transformed into crystallite or microcrystalline material through recrystallisation, forming new minerals. The devitrification process comprises vitreous dissolution and precipitation, recrystallisation, migration and transformation of metal ions, and a series of geochemical processes (Kirov, Samajova, & Nedialkov, 2011; McHenry, 2009). The formation of new minerals is associated with volume decrease, and thus a large number of micropores can be formed between the different minerals.

Devitrification of glass is affected by various geological factors, such as formation temperature, pressure, pH, fluid composition and velocity. Experimental studies by Aradóttir, Sigfússon, Sonnenthal, Björnsson, and Jónsson (2013), Declercq, Diedrich, Perrot, Gíslason, and Oelkers (2013), Gíslason and Oelkers (2003), and Wolff, Gíslason, Oelkers, and Putnis (2004) have shown that the dissolution rates of glassy basalt (basic) and glassy rhyolite (acidic) decrease dramatically with increasing pH under acid conditions (given a single variable of pH), minimise at near-neutral pH and increase more slowly with increasing pH under basic conditions. Given a single variable of temperature, the higher the temperature, the faster the dissolution rate (Figure 10). Acidic conditions are favourable for the dissolution of natural Al-silicate volcanic glasses, removal of metals from the glass structure via proton exchange reactions, and precipitation of silica (and therefore, for devitrification). The Tiaohu Formation tuffs are distributed directly below a set of stable mudstones and, therefore, formed within a relatively closed environment with good sealing characteristics. The presence of H^+ in the formations arises mainly from organic acids produced in the evolution of the organic matter.

An exceptionally favourable condition for the high degree of devitrification in the Tiaohu Formation tuffs is the content of a certain amount of sedimentary organic matter. This

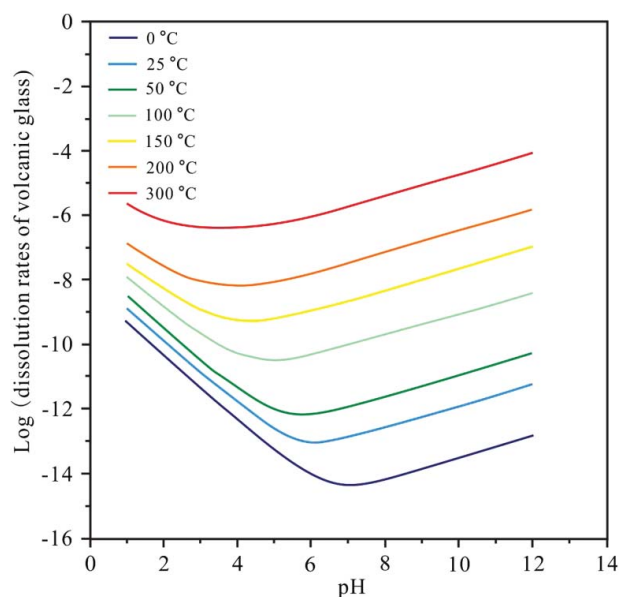


Figure 10. Dissolution rates of volcanic glass at temperatures from 0–300 °C and pH from 1–12 (modified after Aradóttir et al., 2013; Gíslason & Oelkers, 2003).

produced organic acids during the thermal evolution, which promoted devitrification. One reason for the rich production of sedimentary organic matter could be that nutrients released rapidly into the water by volcanic ash are favourable for promoting biological blooms (Delmelle, Lambert, Dufrière, Gerin, & Óskarsson, 2007; Langmann, Zakšek, Hort, & Duggen, 2010; Lin et al., 2011). Another reason could be that volcanic ash might cause the death of lacustrine creatures, resulting in the rapid burial of hydrocarbon-generating material. Furthermore, the fine size and large specific surface area of volcanic ash enable it to absorb a range of dissolved and granular organic matter. Moreover, pyrite is observed in the tuff cores, which suggests a reducing environment that was favourable for the preservation of organic matter (Demailson & Moore, 1980; Graciansky, Deroo, Herbin, & Magniez, 1984; Ma et al., 2015).

The characteristics of high porosity and low permeability are related to the devitrification of volcanic glass in the tuff. Individual interparticle pores within the tuff, produced by devitrification, have small sizes but are large in number, resulting in high overall porosity. With a positive correlation between permeability and pore throat radius, the fine granularity and small pore throat radii (0.003–0.286 μm) of the tuff result in a very low permeability.

Evolution of tuff porosity

As interparticle pores between the minerals formed by devitrification are the principal pore type within the tuff, if the contents of the main minerals such as quartz and feldspar were known, porosity produced during devitrification can then be calculated using the back-stepping method.

Model for calculation of porosity produced during devitrification. The porosity produced during devitrification can be

Table 3. Main mineral composition, corresponding mole mass and proportion of substance.

Mineral	Chlorite	Sodium feldspar	Potassium feldspar	Calcite	Quartz
Mass fraction (%)	m1	m2	m3	m4	m5
Molecular formula	(FeMgAl) ₆ [(SiAl) ₄ O ₁₀](OH) ₈	NaAlSi ₃ O ₈	KAlSi ₃ O ₈	CaCO ₃	SiO ₂
Mole mass (g/mol)	1158	262	278	100	60
Amount of substance proportion	a	b	c	d	1

calculated from mineral compositions, determined by XRD analysis and major element compositions, determined by X-ray fluorescence analysis, combined with the principle of mass conservation (e.g. Zhao et al., 2009). If there are many crystal pyroclasts and detritus, they should be eliminated from the calculations. The specific procedures are as follows.

First, the main mineral composition is determined. The tuff mainly consists of quartz, feldspar and small amount of clay minerals (mainly chlorite). The following uses these three types of mineral as an example.

Second, using Table 3, the amount (number of moles) of all the minerals are calculated (assuming for quartz, the number of moles = 1) using Equations 1–4:

$$a = \frac{m1}{1158} \times \frac{60}{m5} \quad (1)$$

$$b = \frac{m2}{262} \times \frac{60}{m5} \quad (2)$$

$$c = \frac{m3}{278} \times \frac{60}{m5} \quad (3)$$

$$d = \frac{m4}{100} \times \frac{60}{m5} \quad (4)$$

Then, the major element compositions of the tuff (Table 4) are allotted to the main minerals of today, according to the order: chlorite first, followed by feldspar (sodium feldspar and potassium feldspar), and quartz (see Equations 5–10):

$$\text{If } \frac{2 \times M4}{160} + \frac{M5}{72} < \frac{M7}{40}, \quad Ma = 1158 \times a \times \left(\frac{2 \times M4}{160} + \frac{M5}{72} \right) \quad (5)$$

$$\text{If } \frac{2 \times M4}{160} + \frac{M5}{72} > \frac{M7}{40}, \quad Ma = 1158 \times a \times \left(\frac{M7}{40} \right) \quad (6)$$

Define that the smaller of $\frac{2 \times M4}{160}$ and $\frac{M5}{72}$ is equal to A.

$$Mn = 262 \times b \times \frac{2 \times M9}{62} \quad (7)$$

Define $\frac{2 \times M9}{62} = N$

$$Mk = 278 \times c \times \frac{2 \times M10}{94} \quad (8)$$

$$\text{Define } \frac{2 \times M10}{94} = K$$

$$Mc = 100 \times d \times \frac{M8}{56} \quad (9)$$

$$Mq = 60 \times \left(\frac{M1}{60} - \frac{2A}{3} - 3N - 3K \right) \quad (10)$$

where Ma, Mn, Mk, Mc and Mq refer to the mass of chlorite, sodium feldspar, potassium feldspar, calcite and quartz, respectively.

Finally, based on mineral density (Table 5), the porosity produced during devitrification is calculated using Equation 11. The original volcanic ash of the tuff is of primarily intermediate–acid nature (Ma, Huang, & Liang, 2016), and the density of intermediate–acid volcanic ash is typically 2.36 g/cm³ (Yang, Shi, Chen, Chen, & Zhang, 2006; Zhao et al., 2009).

$$\phi 1 = 1$$

$$- \left(\frac{Ma}{2.7} + \frac{Mn}{2.62} + \frac{Mk}{2.59} + \frac{Mc}{2.71} + \frac{Mq}{2.65} \right) / \left(\frac{M}{2.36} \right) \quad (11)$$

Porosity of the vitric and crystal-vitric tuffs is calculated separately because of the great difference between them. Figure 11a shows that the porosity produced during devitrification of both tuffs increases with depth, but the rate of increase for the vitric tuff is faster and stops increasing at deeper depths. It is speculated that vitric tuff porosity might increase further, even at depths >3000 m. Crystal-vitric tuff

Table 4. Major element compositions of the tuff and corresponding mole masses.

Major element	SiO ₂	TiO ₂	Al ₂ O ₃	Fe ₂ O ₃	FeO	MnO	MgO	CaO	Na ₂ O	K ₂ O	Total
Mass fraction (%)	M1	M2	M3	M4	M5	M6	M7	M8	M9	M10	M
Mole mass (g/mol)	60	80	102	160	72	71	40	56	62	94	

$$M = M1 + M2 + \dots + M9 + M10$$

Table 5. Density of mineral composition of the tuff and primary volcanic ash.

Mineral	Quartz	Sodium feldspar	Potassium feldspar	Chlorite	Calcite	Volcanic ash
Density (g/cm ³)	2.65	2.62	2.59	2.70	2.71	2.36

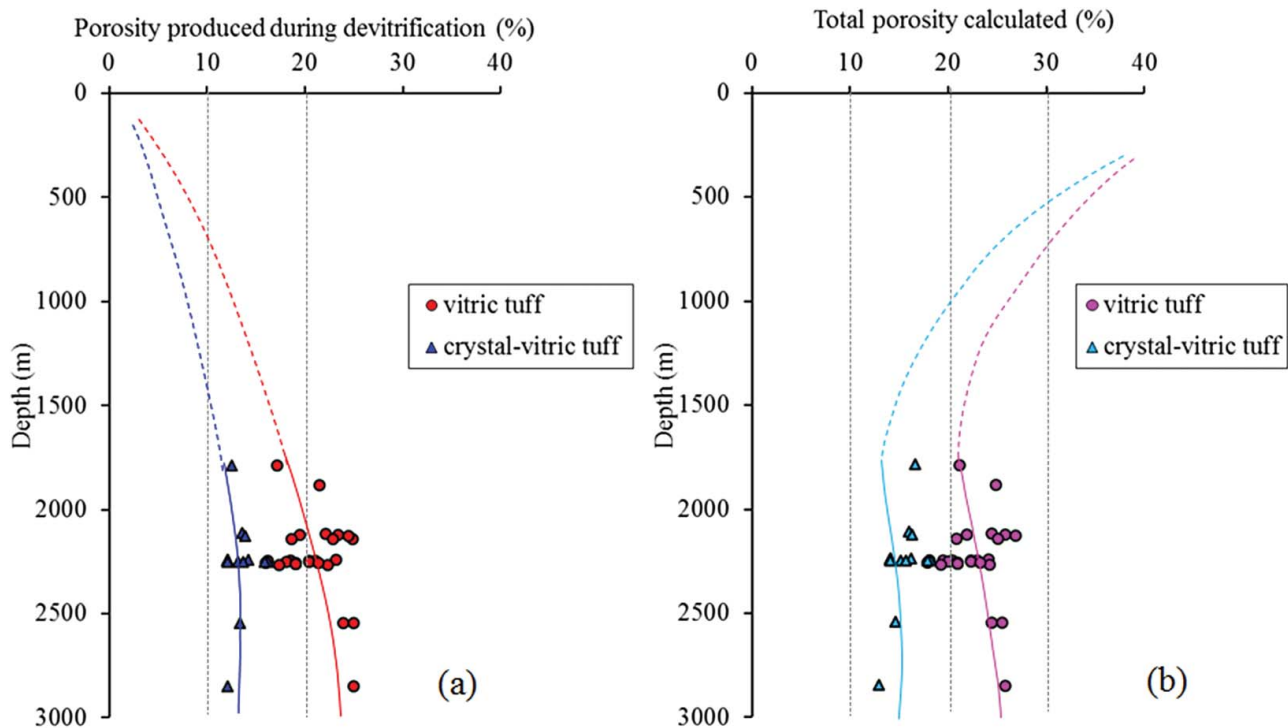


Figure 11. Characteristics of porosity evolution of different types of tuff: (a) evolution of porosity produced during devitrification; and (b) evolution of total calculated porosity.

porosity initially increases with depth but then stabilises and remains constant at depths >2600 m. This is because the original volcanic ash determines the process of devitrification, and the greater the content of vitroclasts, the higher the degree of devitrification.

Characteristics of porosity evolution. Owing to the fine particles of air-fall volcanic ash, similar to mudstone, the formation of tuff actually incorporates two processes: normal compaction of fine-grained sediments and devitrification of volcanic glass. Compaction is a porosity-reducing process, whereas devitrification is a process that increases porosity. The compaction curve of tuffs can be replaced by the compaction curve of mudstones, which are also fine-grained sediments. Compaction porosity can be calculated using the logging data of interval transit time from the mudstone and tuffaceous mudstones above the tuff (Figure 12), and the relation between porosity and depth is expressed as (see Equation 12):

$$\phi_2 = 0.7 \times e^{-0.0016H}, \quad (12)$$

where ϕ_2 is the compaction residual porosity, and H is burial depth (m).

Adding the compaction residual porosity and the porosity produced during devitrification, the total porosity of different types of tuffs can be calculated. The calculated porosity matches the measured porosity well (Figure 13a). Among the single minerals, there is good correlation between the

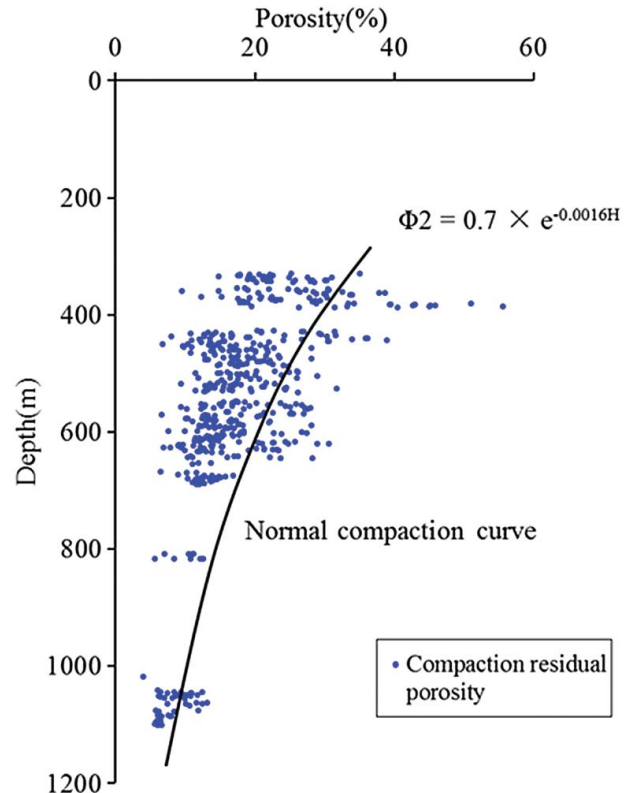


Figure 12. Correlation between compaction residual porosity and depth, showing the porosity decreases with the increase in the depth. The compaction residual porosity is calculated using the logging data of interval transit time from the mudstone and tuffaceous mudstones above the tuff.

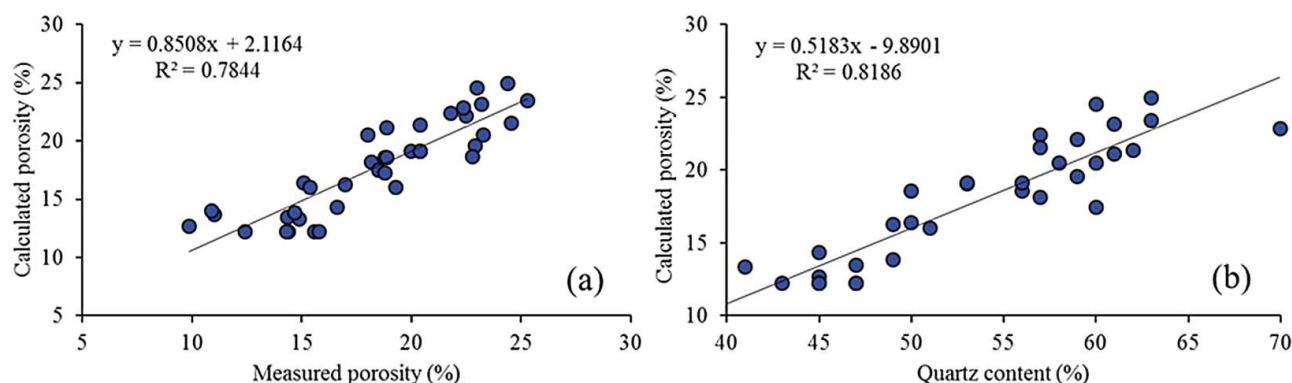


Figure 13. (a) Correlation between calculated porosity and measured porosity and (b) correlation between calculated porosity and quartz content in the Tiaohu Formation tuffs.

calculated porosity and quartz content (Figure 13b). This shows that tuff porosity can be speculated based on the quartz content, because quartz is the principal leading mineral in the devitrification of the Tiaohu Formation tuffs.

The characteristics of porosity evolution of the vitric and crystal-vitric tuffs are similar; porosity initially decreases and then increases with increasing depth (Figure 11b). When the depth is shallow compaction dominates, reducing porosity, but as depth increases, the impact of devitrification outweighs the effect of compaction, and porosity increases. The porosity of vitric tuff is higher than crystal-vitric tuff at the same depth. The rate of decrease in crystal-vitric tuff porosity with increasing depth is larger than vitric tuff in shallow strata, and the rate of increase in crystal-vitric tuff porosity with increasing depth is smaller than vitric tuff in deep strata. For depths >3000 m, vitric tuff retains the trend of high porosity, but the porosity of crystal-vitric tuff shows almost no change at depths >2600 m, or even decreases. Therefore, the degree of devitrification is controlled by both the original composition and the burial depth of the tuff.

Conclusions

The tight oil reservoir of the Santanghu Basin is peculiar in that the reservoir is a tuff and not shale, sandstone or carbonate. A thorough analysis of its formation characteristics and reservoir potential is of considerable importance regarding the exploration for, and exploitation of, other similar resources. However, the quantitative research of the devitrification of the tuff still requires further investigation.

- (1) Matrix-related pores in tuffs are mainly interparticle pores between minerals and intraparticle pores within minerals formed during devitrification. The pores are difficult to observe under an ordinary microscope; however, well-developed micron–nanometer-scale pores were found in large numbers under SEM and CT scanning.
- (2) Based on distance from the volcanic activity belt and compositional differences, the tuffs were divided into vitric, crystal-vitric, pelitic and silicified tuffs,

characterised by high porosity and big throat, moderate porosity and thin throat, low porosity and thin throat, and very low porosity and moderate throat pore structures, respectively.

- (3) The tuff of the Permian Tiaohu Formation in the Santanghu Basin contains sedimentary organic matter; extracted tuff samples have TOC values of 0.5–1.0 wt%, and the organic matter comprises mainly Types III and II₂ kerogen. Organic acids produced during kerogen maturation facilitate the process of devitrification and the formation of reservoir micropores. The tuff reservoir is characterised by high porosity and low permeability, of which vitric tuff has the best reservoir properties.
- (4) Tuff porosity evolution is controlled mainly by original composition and burial depth. The porosity of vitric tuff is higher than crystal-vitric tuff at the same depth, but both their porosities are characterised by an initial decrease and then an increase with increasing depth. For depths >3000 m, vitric tuff retains the trend of high porosity, but the porosity of crystal-vitric tuff scarcely changes or even decreases.

Acknowledgements

This research was supported financially by the National Natural Science Foundation of China (No.: 41472111). The authors thank the PetroChina Turpan-Hami Oilfield Company for providing valuable geological data, as well as the crude oil and core samples.

Disclosure statement

No potential conflict of interest was reported by the authors.

Funding

National Natural Science Foundation of China [grant number 41472111]

References

- Aradóttir, E. S. P., Sigfússon, B., Sonnenthal, E. L., Björnsson, G., & Jónsson, H. (2013). Dynamics of basaltic glass dissolution–capturing

- microscopic effects in continuum scale models. *Geochimica et Cosmochimica Acta*, 121, 311–327.
- Clarkson, C. R., & Pedemen, P. K. (2011). *Production analysis of western Canadian unconventional light oil plays*. Richardson, Tx: Society of Petroleum Engineers 149005.
- d'Atri, A. D., Dela Pierre, F. D., Lanza, R., & Ruffini, R. (1999). Distinguishing primary and resedimented vitric volcanoclastic layers in the Burdigalian carbonate shelf deposits in Monferrato (NW Italy). *Sedimentary Geology*, 129, 143–163.
- Declercq, J., Diedrich, T., Perrot, M., Gíslason, S. R., & Oelkers, E. H. (2013). Experimental determination of rhyolitic glass dissolution rates at 40–200 °C and $2 < \text{pH} < 10.1$. *Geochimica et Cosmochimica Acta*, 100, 251–263.
- Delmelle, P., Lambert, M., Dufrène, Y., Gerin, P., & Óskarsson, N. (2007). Gas/aerosol-ash interaction in volcanic plumes: New insights from surface analyses of fine ash particles. *Earth and Planetary Science Letters*, 259, 159–170.
- Demaison, G. J., & Moore, G. T. (1980). Anoxic environments and oil source bed genesis. *Organic Geochemistry*, 2, 9–31.
- Fic, J., & Pedersen, P. K. (2013). Reservoir characterization of a 'tight' oil reservoir, the middle Jurassic Upper Shaunavon Member in the White-mud and Eastbrook pools, SW Saskatchewan. *Marine and Petroleum Geology*, 44, 41–59.
- Gao, G., Li, H. M., & Liang, H. (2010). Origin of Jurassic hydrocarbon and accumulation model in Santanghu Basin. *Natural Gas Geoscience*, 21, 15–18 (in Chinese with English abstract).
- Gíslason, S. R., & Oelkers, E. H. (2003). Mechanism, rates and consequences of basaltic glass dissolution: An experimental study of the dissolution rates of basaltic glass as a function of pH and temperature. *Geochimica et Cosmochimica Acta*, 67, 3817–3832.
- Gong, Q. S., Ni, G. H., & Lu, S. P. (2010). Genesis and reservoir features of tuffaceous rocks in Wuerhe oilfield of the Junggar Basin. *Oil and Gas Geology*, 31, 481–485 (in Chinese with English abstract).
- Graciansky, P. C. De., Deroo, G., Herbin, J. P., & Magniez, L. (1984). Ocean-wide stagnation episode in the late Cretaceous. *Nature*, 22, 346–349.
- Haaland, H. J., Furnes, H., & Martinsen, O. J. (2000). Paleogene tuffaceous intervals, Grane Field (Block 25/11), Norwegian North Sea: Their depositional, petrographical, geochemical character and regional implications. *Marine and Petroleum Geology*, 17, 101–118.
- Huff, W. D. (2008). Ordovician K-bentonites: Issues in interpreting and correlating ancient tephras. *Quaternary International*, 178, 276–287.
- Jia, C. Z., Zheng, M., & Zhang, Y. (2012a). Unconventional hydrocarbon resources in China and the prospect of exploration and development. *Petroleum Exploration and Development*, 39, 139–146.
- Jia, C. Z., Zou, C. N., Li, J. Z., Li, D. H., & Zheng, M. (2012b). Assessment criteria, main types, basic features and resource prospects of the tight oil in China. *Acta Petrolei Sinica*, 33, 343–350.
- Jiao, L. X., Liu, J. T., Zhang, H., Feng, Y. Q., & Wu, C. (2014). Tight reservoir characteristics and formation conditions of tuff in Santanghu Basin. *Natural Gas Science*, 25, 1697–1705.
- Kirov, G., Samajova, E., & Nedialkov, R. (2011). Alteration processes and products of acid pyroclastic rocks in Bulgaria and Slovakia. *Clay Minerals*, 46, 279–294.
- Kolata, D. R., Frost, J. K., & Huff, W. D. (1987). Chemical correlation of K-bentonite beds in the Middle Ordovician Decorah subgroup, upper Mississippi valley. *Geology*, 15, 208–211.
- Königer, S., Lorenz, V., Stollhofen, H., & Armstrong, R. A. (2002). Origin, age and stratigraphic significance of distal fallout ash tuffs from the Carboniferous–Permian continental Saar-Nahe basin (SW Germany). *International Journal of Earth Sciences*, 91, 341–356.
- Kuhn, P. P., di Primio, R., Hill, R., Lawrence, J. R., & Horsfield, B. (2012). Three-dimensional modeling study of the low-permeability petroleum system of the Bakken Formation. *AAPG Bulletin*, 96, 1867–1897.
- Langmann, B., Zakšek, K., Hort, M., & Duggen, S. (2010). Volcanic ash as fertiliser for the surface ocean. *Atmospheric Chemistry and Physics*, 10, 3891–3899.
- Li, D. H., Li, J. Z., Huang, J. L., Wang, S. Y., & Wang, S. F. (2014). An important role of volcanic ash in the formation of shale plays and its inspiration. *Natural Gas Industry*, 34, 56–65 (in Chinese with English abstract).
- Liang, H., Li, X. N., Ma, Q., Xiang, H., Luo, Q. S., & Chen, X. (2014). Geological features and exploration potential of Permian Tiaohu Formation tight oil, Santanghu Basin, NW China. *Petroleum Exploration and Development*, 41, 563–572.
- Lin, I. I., Hu, C. M., Li, Y. H., Fischer, T. P., Wong, G. T. F., & Wu, J. F. (2011). Fertilization potential of volcanic dust in the Low-nutrient low-chlorophyll western North Pacific subtropical gyre: Satellite evidence and laboratory study. *Global Biogeochemistry Cycles*, 25, 1–12.
- Liu, Y. Q., Li, H., & Zhu, Y. S. (2010). Permian lacustrine eruptive hydrothermal dolomites, Santanghu basin, Xinjiang province. *Acta Sedimentologica Sinica*, 28, 861–865 (in Chinese with English abstract).
- Loucks, R. G., Reed, R. M., Ruppel, S. C., & Hammes, U. (2012). Spectrum of pore types and networks in mudrocks and a descriptive classification for matrix-related mudrock pores. *AAPG Bulletin*, 96, 1071–1098.
- Ma, J., Huang, Z. L., Gao, X. Y., & Chen, C. C. (2015). Oil-source rock correlation for tight oil in tuffaceous reservoirs in the Permian Tiaohu Formation, Santanghu Basin, northwest China. *Canadian Journal of Earth Sciences*, 52, 1014–1026.
- Ma, J., Huang, Z. L., Li, H. M., & Wu, H. Z. (2012). Matching relationship between faults and source rock and vertical migration characteristics of the oil in the Malang sag. *Acta Sedimentologica Sinica*, 30, 1140–1148 (in Chinese with English abstract).
- Ma, J., Huang, Z. L., & Liang, S. J. (2016). Geochemical and tight reservoir characteristics of sedimentary organic-matter-bearing tuff from the Permian Tiaohu Formation in the Santanghu Basin, Northwest China. *Marine and Petroleum Geology*, 73, 405–418.
- Ma, M. F., Li, W., & Liu, Y. C. (2005). Pore structure characteristics analysis of the oilfield in north Melut Basin, Sudan. *Petroleum Exploration and Development*, 32, 121–124.
- McHenry, L. J. (2009). Element mobility during zeolitic and argillic alteration of volcanic ash in a closed-basin lacustrine environment: Case study Olduvai Gorge, Tanzania. *Chemistry Geology*, 265, 540–552.
- Qiu, X. W., Liu, C. Y., Mao, G. Z., Deng, Y., Wang, F. F., & Wang, J. Q. (2014). Late Triassic tuff intervals in the Ordos basin, Central China: Their depositional, petrographic, geochemical characteristics and regional implications. *Journal of Asian Earth Sciences*, 80, 148–160.
- Qiu, X. W., Liu, C. Y., Mao, G. Z., & Wu, B. L. (2011). Petrological-geochemical characteristics of volcanic ash sediments in Yanchang Formation in Ordos Basin. *Earth Science-Journal of China University of Geosciences*, 36, 139–150 (in Chinese with English abstract).
- Thompson, M. D., & Hermes, O. D. (1990). Ash-flow stratigraphy in the Mattapan Volcanic Complex, greater Boston, Massachusetts. *Geological Society of America Special Papers*, 245, 85–96.
- Tissot, B., & Welte, D. H. (1984). *Petroleum formation and occurrence*. Berlin: Springer Verlag.
- Wang, P., Pan, J. G., & Wei, D. T. (2011). A new type of hydrocarbon source rock-sedimentary tuff. *Journal of Xi'an Shiyu University*, 26, 19–22 (in Chinese with English abstract).
- Wolff, D., Gíslason, S. R., Oelkers, E. H., & Putnis, C. V. (2004). The dissolution rates of natural glasses as a function of their composition at pH 4 and 10.6, and temperatures from 25 to 74 °C. *Geochimica et Cosmochimica Acta*, 68, 4843–4858.
- Xiao, W. J., Windley, B. F., Badarch, G., Sun, S., Li, J. L., Qin, K. Z., & Wang, Z. H. (2004a). Palaeozoic accretionary and convergent tectonics of the southern Altai: Implications for the growth of Central Asia. *Journal of the Geological Society*, 161, 339–342.
- Xiao, W. J., Zhang, L. C., Qin, K. Z., Sun, S., & Li, J. L. (2004b). Palaeozoic accretionary and collisional tectonics of the Eastern Tianshan (China): Implications for the continental growth of central Asia. *American Journal of Science*, 304, 370–395.
- Xu, H., Tang, D. Z., & Zhang, J. F. (2013). Coexistence mechanism of multi-types of reservoir pressure in the Malang depression of the Santanghu basin, China. *Journal of Petroleum Science and Engineering*, 108, 279–287.
- Yang, Q. F., Shi, L. B., Chen, X. D., Chen, B., & Zhang, Y. (2006). Characteristics of recent ejecta of the Changbaishan Tianchi volcano,

- China. *Seismology and Geology*, 28, 71–83 (in Chinese with English abstract).
- Zhao, H. L., Huang, W., Wang, C., & Di, Y. J. (2009). Micropores from devitri-fication in volcanic rocks and their contribution to reservoirs. *Oil and Gas Geology*, 30, 47–52 (in Chinese with English abstract).
- Zhao, X. Z., Li, Q., Jiang, Z. X., Zhang, R. F., & Li, H. P. (2013). Organic geo-chemistry and reservoir characterization of the organic matter-rich calcilutite in the Shulu Sag, Bohai Bay Basin, North China. *Marine and Petroleum Geology*, 51, 239–255.
- Zhu, Y. F., Zhang, L. F., Gu, L. B., & Guo, X. (2005). The zircon shrimp chro-nology and trace element geochemistry of the carboniferous volcanic rocks in western Tianshan Mountains. *Chinese Science Bulletin*, 50, 2201–2212.